IAC-11-B2.6.2

Free-space laser communications for satellite downlinks: Measurements of the atmospheric channel

Florian Moll
German Aerospace Center, Germany, florian.moll@dlr.de

Markus Knapek
German Aerospace Center, Germany, markus.knapek@dlr.de

Future satellite communications can benefit greatly from the usage of frequencies in the optical spectrum. These allow data-rates comparable to fiber optical communications and provide additional advantages over traditional radio-frequency carriers like more power efficiency, small weight and size, and usage of frequency bands without ITU regulation. However, optical satellite downlinks are affected by the degradation of signal quality due to atmospheric turbulence. In fact, a profoundly verified channel model for this scenario does not exist yet, as there is no satisfying database of channel measurements so far. To contribute in disposing this lack of data, the Optical Communications Group at DLR performed laser downlinks from the Japanese OICETS to the DLR Optical Ground Station in Oberpfaffenhofen near Munich, Germany, in 2006 and 2009. The trials in 2006 were in cooperation with JAXA, NICT and DLR, whereas in 2009 they were part of a downlink-campaign comprising JAXA, NICT, ESA, NASA/JPL, and DLR. Measurements of intensity scintillations and wave-front distortions were undertaken that show the development of atmospheric turbulence over the elevation angle. Measurement devices like the differential image motion monitor, pupil camera, Shack-Hartmann wave-front sensor, and power meters were applied. Metrics that may be derived from the measurements are Fried parameter, scintillation index, intensity correlation length, and complex wave-front. The measurements may support the refinement of the common channel models. The applied communication scheme was a 50-Mbit/s on-off keying at a wavelength of 847 nm. Bit-error rates were recorded in parallel to the atmospheric measurements. In ten trials out of eighteen, signals were received while the others were hindered by cloud blockage. Seven of these trials were found to have useful data for analysis. The elevation angle of the analyzed links ranges between 4 and 55 deg. The present paper contains a description of the experiments in 2006 and 2009 and highlights the results so far. In this paper, the setup of the optical ground station is outlined as well as the measurement devices and results. Emphasis is put on analysis of the measurements of received optical power and complex wave-fronts.

I. INTRODUCTION

The technology of free-space optical links in satellite communications is at a level where it is expected to be close to being operational within the next years when the European Data Relay Satellite System (EDRS) will apply laser communication terminals for its inter-satellite-links[1,2]. Besides the advantages of laser communication, the acquisition, pointing, and tracking of the counter-terminals is one of the biggest challenges in this scenario. Furthermore, the atmosphere, and here especially the troposphere, may have a big impact. The influence can be as severe as having clouds blocking a link completely or atmospheric turbulence degrading signal quality down to a very low level. Investigations are undertaken in forming sophisticated models based on theory and measurements of the atmospheric conditions. Models may be derived from plain theory, measurements, or a combination of both. Application of plain theory has the drawback, that there are closed mathematical solutions for only a subset of problems, i.e. certain assumptions and simplifications always occur. Measurements take in the cumulated effects that appear on the channel and show how reality can be. However, they must match existing theory and side effects must be concerned about. Thus, measurements coinciding and together with common theory are the best choice for a model describing channel behavior in the satellite-ground link. In this paper, we present an analysis of channel measurements of downlinks between a low Earth orbiting satellite and an optical ground station at mid-latitudes, i.e. Munich, Germany.

The Japan Aerospace Exploration Agency (JAXA) has built the Optical Inter-orbit Communications Engineering Test Satellite (OICETS) which was launched from Baikonur Cosmodrome in 2005. Payload is the Laser Utilization Communications Equipment (LUCE) which is programmable to either perform inter-satellite links or satellite-ground links. For the OICETS-ground scenario, transmitted data is a PN code at 49.3724Mbps with modulation format on/off-keying at 847nm transmission wavelength at 100mW output power[3,4]. To maintain a stable link, optical tracking on satellite and ground station side was applied. In 2006, first downlinks were demonstrated to an optical ground station in Tokyo, run by NICT (National Institute of Information and Communications Technology)[5]. The first European downlinks were then conducted later in 2006 within the work of the DLR (German Aerospace

Center) project KIODO (KIrari's Optical Downlink to Oberpfaffenhofen)[6,7]. Eight trials were performed. In five of them, a link could be established. This campaign was repeated in 2009 with some extensions in the framework of a global downlink campaign involving JAXA, NICT, ESA (European Space Agency), JPL (Jet Propulsion Laboratory), and DLR and to some extent, analysis and application of gathered data has been published[8,9,10,11,12]. Between June and September in 2009, ten downlinks to the optical ground station at DLR Oberpfaffenhofen were planned, whereas in five signals could be received. Regarding successful data recording, altogether seven of these experiments are used for analysis. Table 1 lists the dates and times of these experiments. All measurements took place during spring/summer at nighttime between midnight and two o'clock (UTC).

Date	Time [UTC]	Exp. designation
9th June 2006	00:00:24	KT06-02
14th June 2006	01:02:51	KT06-03
15th June 2006	23:52:10	KT06-04
1st July 2009	01:28:12	KT09-03
19th August 2009	02:20:34	KT09-05
21st August 2009	01:02:50	KT09-06
28th August 2009	02:04:38	KT09-08

Table 1: List of analyzed experiments. The designation contains the year of measurement and sequential numbering of the two campaigns. The time corresponds to 1° pointing elevation.

In the following, first, a brief explanation of the effects of atmospheric turbulence is given. Then, the performed measurements are described and its analysis presented. The behavior of the link channel in terms of power scintillation, temporal correlation, fade statistics, and phase distortion for our example system will be given. Direct comparison of the measurements to the common theoretic models is not within the scope of this paper and will be published elsewhere.

II. THEORY OF ATMOSPHERIC TURBULENCE

The early studies of turbulence in the atmosphere were undertaken by investigating the velocity field of a viscous fluid[13] and have later been applied to temperature fluctuations and finally index of refraction fluctuations[14]. The strength of these fluctuations is described by the atmospheric parameter index of refraction structure constant C_n^2 [$m^{-2/3}$]. This is the proportionality factor in the structure function $D_n(R)$ [-], where $n_{1,2}$ [-] is index of refraction at two locations with separation distance R [m].

$$D_n(R) = \left\langle \left(n_1 - n_2\right)^2 \right\rangle = C_n^2 R^{2/3} \qquad [1]$$

With increasing local deviations of $n_{1,2}$ at a fixed separation, the structure constant increases which means stronger turbulence, thus higher C_n^2. With increasing altitude above ground, strength of turbulence falls down till top of atmosphere except for a bump at Tropopause level. The severity of the cumulated turbulence along the downlink path can be put in numbers via the Rytov variance for a plane wave σ_R^2 [-].

$$\sigma_R^2 = 2.25 k^{7/6} \int_0^L C_n^2(z) \cdot z^{5/6} dz \qquad [2]$$

Here, L [m] is the path length through the atmosphere, k [m^{-1}] the circular wave number and z [m] the path variable. With higher values of the integration core, the cumulated turbulence increases. This means, for the downlink scenario, at low elevations turbulence is higher, because the longer propagation path through the turbulent layer, whereas at high elevations turbulence is lower. A parameter that is more related to the actual system is the power scintillation index (PSI) σ_P^2 [-]. It gives a measure for the fluctuation of power received by the telescope on ground and is expressed as the normalized variance of received power P [W]. The brackets in equation 1 denote ensemble averages.

$$\sigma_p^2 = \frac{\left\langle P^2 \right\rangle - \left\langle P \right\rangle^2}{\left\langle P \right\rangle^2} \qquad [3]$$

The power scintillation index depends on the system aperture, the link distance, and the Rytov variance. The atmospheric turbulence causes a distortion of the electro-magnetic wave which results in intensity speckles in cross section of the laser beam. For a very short time, in the order of milliseconds, these speckles are considered to be static due to the Taylor frozen turbulence hypothesis[13]. Therefore, the spatial characteristics of the beam can be translated to temporal behavior assuming the turbulence is blown across the receiver aperture by wind or the beam crossing the atmosphere with the slew rate of the satellite.

This paper describes the channel measurements undertaken in the two campaigns 2006 and 2009. The forthcoming chapter outlines the applied measurement instruments and setup.

III. MEASUREMENT INSTRUMENTS

The optical ground station can be flexibly equipped and usually hosts various measurement and test devices. Two partly different instrument setups were used for the campaigns in 2006 and 2009. The main characteristics of the ground station are listed in Table 2. An overview of the applied instruments is given in Table 3. Devices like the differential image motion monitor (DIMM)[15],

pupil camera[16] and the Shack-Hartmann wave-front sensor[17] (SHWFS) are widely used in turbulence characterization and beam profiling and chosen to be suitable for the concerned scenario. Fig. 1 shows an image of the OGS with hosted telescope mount.

Geographical location	48.082° N, 11.276° E
Height above sea level	645m
Height above ground	11m
Dome	4m clamshell
Telescope type	40cm Cassegrain

Table 2: Main characteristics of Optical Ground Station Oberpfaffenhofen (OGSOP).

Fig. 1: Optical ground station at the German Aerospace Center Oberpfaffenhofen.

The two power meters with aperture size 5cm and 40cm sample the optical power integrated over the telescope aperture. The bit error rate tester (BERT) is applied to measure the actual bit error rate of the received signal format. The differential image motion monitor is a typical turbulence characterizing instrument very common in Astronomy. It basically captures two focus spots on one camera chip that show differential movement due to the turbulence. From this motion, the Fried parameter can be derived. The pupil camera captures images of the intensity distribution of the optical systems exit pupil. With these images, the statistics of the pupil plane intensity speckles and scintillation are derived. Furthermore, it is possible to calculate C_n^2-profiles. The focus camera acquires images of the instantaneous focus spot and can be used as cross-check to the wave-front sensor or to derive the Fried parameter applying different methods. The Shack-Hartmann wave-front sensor (SHWFS) results the complex field of the wave. The data logger samples the data in high bandwidth, i.e. 250 MSamples and 8bit resolution. These measurements are used for simulating behavior of different receiver parameters on data reception.

Sequence of link establishing of the ground station is performed in three stages. First, OICETS and OGS point to each other via open loop control whereas OGS makes use of the newest CPF files. The OGS sends the beacon beams (807.8 and 809.1nm, ~5mrad divergence each) towards the predicted orbit of the satellite. After having detected the beacons, OICETS starts emitting the laser beam towards the ground station (second step). In the third step, the mutual alignment is maintained via optical tracking. Therefore, the OGS applies a wide field of view tracking camera attached to the side of the receiver telescope, and a narrow field of view (NVOW) camera, installed on the optical bench. During the link, the signals of the particular instruments are recorded with synchronized time stamps. Although, uplink communication with OICETS would be possible, only the downlink is performed. Fig. 2 shows the optical setup as it was designed for the 2009 campaign[18]. This setup is mounted on an optical aluminum bench flanged to the telescope back.

Measurement	Campaign
Power meter	2006/2009
BERT	2006/2009
DIMM	2006/2009
Focus camera	2009
SHWFS	2009
Pupil camera	2006/2009
Data logger	2009
Power meter 5cm	2006/2009

Table 3: List of applied measurement instruments. All instruments are attached to the optical bench of the 40cm Cassegrain Telescope expect for the separate 5cm aperture power meter.

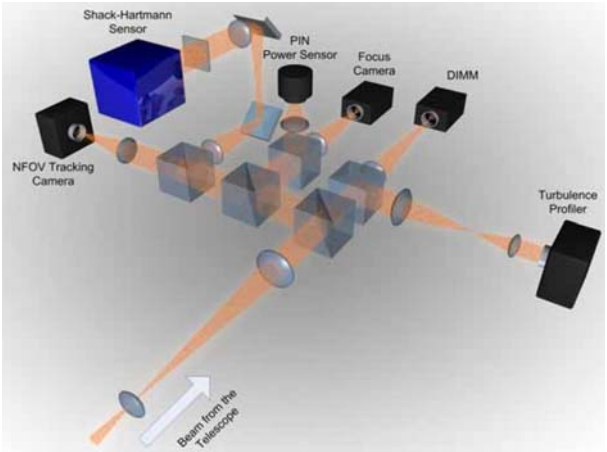

Fig. 2: Instrument setup in the 2009 campaign. The beam is guided to the tracking camera, receiver front-end and measurement instruments.

IV. ANALYSIS

In this chapter, the procedure of measurement analysis and the results of the recorded power on the receiver front-end and Shack-Hartmann images are described. The system aperture diameter for both measurements was 40cm.

IV.I Power measurements

Power measurements were recorded at a sample rate of 10kHz in the campaign 2006 and 20kHz in the campaign 2009. In the first, a Thorlabs PDA55 Si PIN with sensitive area of 3.6x3.6mm was used for power measurements. The field of view was 0.9mrad. In 2009, the applied receiver front-end had a low frequency power indicator signal. The front-end consisted of a Si PIN diode with 1mm diameter. The field of view of this setup was 0.7mrad. In either case, the systems field of view is much larger than the tracking accuracy of the telescope mount (~50µrad) and thus big enough to avoid the focus spot from wandering off the detector. To increase the dynamic of the receiver, a variable optical attenuator, a controllable neutral density filter wheel, was applied in 2009. Signals were recorded by use of a National Instruments DAQ card with 16bit channels.

For analysis of the individual trials, the measurement and orbit data are extracted first. In the preprocessing, noise reduction is performed applying a low-pass filter with pass band till 2kHz. Then, the systematic offset is removed by subtracting background measurements from the signal recordings. Since power fluctuation and mean incident power bears high dynamics, cases of low signal to noise ratio and saturation occur occasionally. Thus, only non-saturated measurements above noise floor are labeled as valid data for analysis. Furthermore, the power records are inspected manually and parts with preposterous data are detected and excluded. For example, this can happen when the captured signal arises from tree backscatter of the beacons or when external light sources are in the field of view. For calculation of the statistics, a sliding window is used. A length of one second is chosen. This is considered to be long enough to let the calculated statistical parameters converge but short enough to avoid averaging out variations of the concerned parameter.

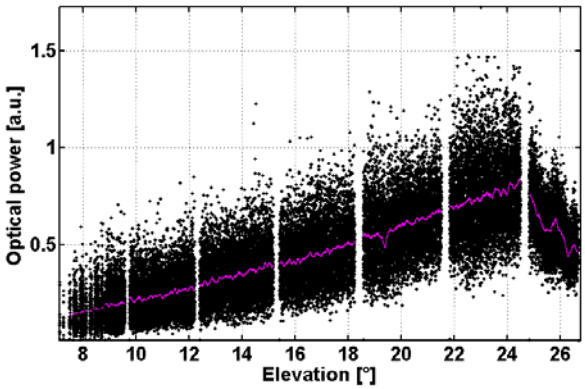

Fig. 3: Received power at KT06-04 in arbitrary units. The black values are the power samples recorded at 10kHz. The magenta line is the 1s sliding window mean.

In Fig. 3, the optical power as it was received in the KT06-04 trial (see Table 1 for explanation of trial numbering) is shown. Please note that arbitrary units are used here, since absolute power is not required for the presented analysis. The sliding mean is illustrated in the magenta line. With increasing elevation, mean power rises due to shorter link distance and lower atmospheric attenuation. Over 24°, a power drop is observed as a result of clouds in the line-of-sight.

The behavior of signal fluctuation over elevation comes out clearer in Fig. 4, where received power is normalized to have unity mean. Signal dynamic is around 16dB at 8° and gets lower with higher elevations, i.e. down to roughly 5dB at 27°. The red curve denotes the fading threshold. In this analysis, a fade is defined as power dropping below 3dB of the instantaneous mean.

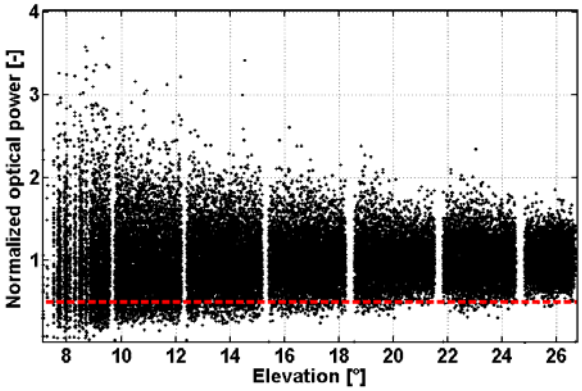

Fig. 4: Normalized received power at KT06-04. The black values are the normalized power samples recorded at 10kHz rate. The dashed red line marks the -3dB threshold with respect to unity mean.

The signal fluctuations are expressed with the power scintillation index. After normalization, the PSI is calculated with

$$\sigma_p^2 = \left\langle P_{norm}^2 \right\rangle - 1 \qquad [4]$$

Fig. 5 shows the same trend of PSI for all measurements. It starts at maximal values up to 0.4 and decreases with growing elevation. Within one measurement, short time variations occur because of local inconsistency of instantaneous C_n^2 profiles. Furthermore, variability is also visible amongst the different down-links. Topography of the surrounding scenery follow, as well as different global meteorological conditions may be the most certain reason. The changeable and unpredictable possible states of the atmosphere are quite clearly illustrated in this overview.

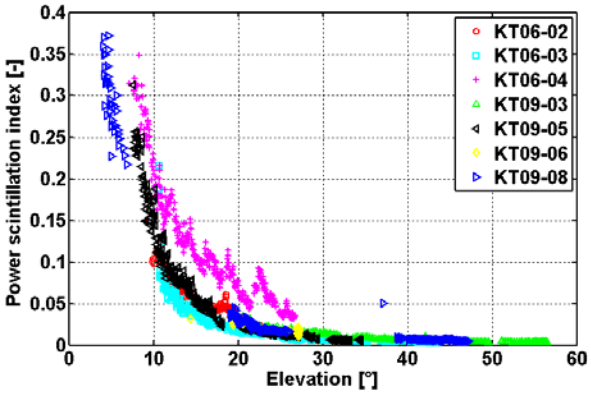

Fig. 5: Power scintillation index for all KIODO measurements.

The corresponding probability density functions of received power recorded in KT06-04 for chosen elevations are calculated and plotted in Fig. . These show the expected log-normal shape. The dashed green line again denotes the defined fading threshold. The area below the curve to its left quantifies the expected fades of the particular over-flight. With higher elevations, the area can decrease significantly.

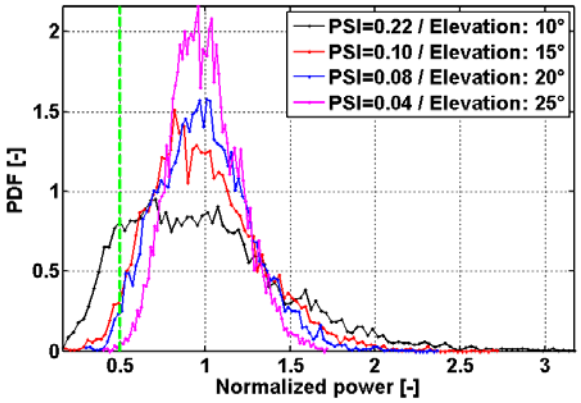

Fig. 6: Probability density functions for selected elevations in KT06-04. The bright green line marks the -3dB threshold with respect to unity mean.

Matching the link elevation of the curve in Fig. , Fig. shows the auto-correlation function (ACF) of the normalized power. As visualized by the dashed red lines, the auto-correlation time of received power (ACT) is defined as the 50% roll-off of the ACF, i.e. the half width of half maximum. The ACT gives a possibility to estimate duration of time the captured power remains in a certain state.

Fig. 8 depicts the overview of ACT over elevation for the analyzed experiments. Changes during the satellite down-links between 0.5ms and 2.5ms are observable. Vertical outliners may occur when the filter wheel changes position or the OICETS/OGS tracking slips or re-acquires. Implementation of excluding these occasions will be done in forthcoming analysis. The measurements prove similar behavior. The ACT is increasing as the satellite goes up and less cumulated turbulence is in the line-of-sight. This causes influence of turbulence to weaken and therefore, the velocity of the power fluctuations to decrease. However, with still higher elevations, slew rate of the satellite accelerates and so the beam through the air volume does which causes power fluctuations to speed up. Depending on instantaneous and maximal link elevation, these two effects work stronger or weaker and thus cause a maximum in the run of the curve of the individual over-flights.

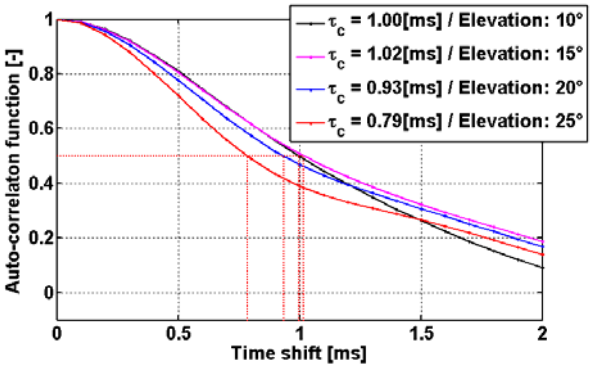

Fig. 7: Auto-correlation functions for selected elevations in KT06-04. The dashed red lines denote the 50% roll-offs.

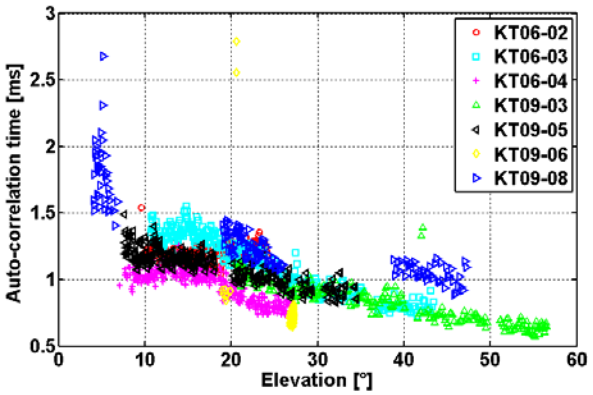

Fig. 8: Auto-correlation time for all KIODO measurements as defined by the 50% roll-off of the auto-correlation function.

Closely related to the PSI and ACT are the fading statistics. In this evaluation, a fade is detected via hard decision of the power being below the defined threshold of -3dB. If a fade occurs, all information bits in its extent are lost, i.e. bit errors evolve. Fig. 9-Fig. 12 give values for the fading behavior in our satellite down-link scenario. The number of fades per unit time (Fig. 9) shows an overall tendency to go down with growing elevation. In the beginning of the satellite passes, fades occur with frequency of 300 times per second due to the

high instantaneous signal dynamics. Due to relatively low dynamics in higher elevations, they almost never occur over 30°.

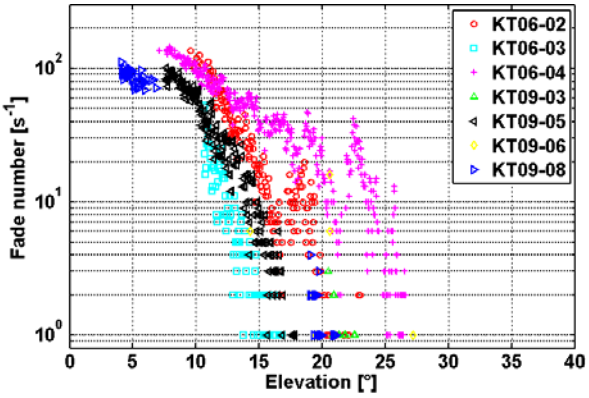

Fig. 9: Absolute number of fades per second for all KIODO measurements. The fade threshold is defined as 3dB below instantaneous mean.

Fade frequency may significantly influence all kinds of acquisition and tracking issues included in the system, e.g. phase tracking, clock recovery, or adaptive optics control loops. The mean fade time varies, with a few exceptions, between 0.1ms and 2.5ms (Fig. 10). Here, the maximum fade length coincides approximately with the maximum ACT. However, minimum fade duration is around five times smaller than minimum ACT. Depending on what is defined as a fade in the actual system, an inter-leaver may, in addition to the ACT, also exploit knowledge of mean fade length for optimal adjustment.

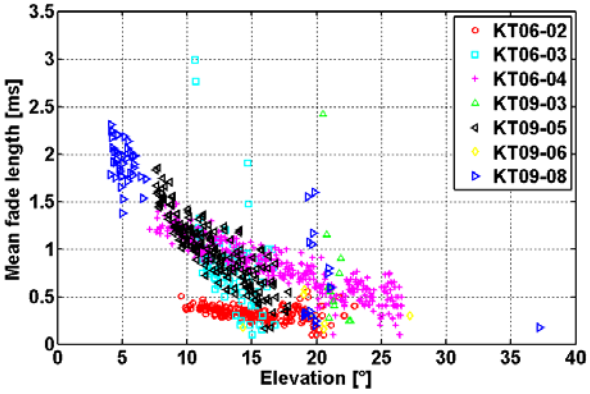

Fig. 10: Mean fade duration for all KIODO measurements. The fade threshold is defined as 3dB below instantaneous mean.

Full information of fading length behavior is given with the cumulative distribution function (CDF) in Fig. . The step like runs of the curves in this representation is caused by the finite sampling rate of the power meter (10kHz in this measurement). The slope of the CDFs go well along with the run of the ACT. For rather low elevations, longer fades occur due higher correlation, whereas at high elevation short correlation times cause shorter fades. Also, maximum and minimum of fade duration are contained in this depiction. However, due to the sampling, minimum can only be roughly estimated to be around 0.1ms for all situations. The maximum fade time, though, varies between 0.9ms and 4ms.

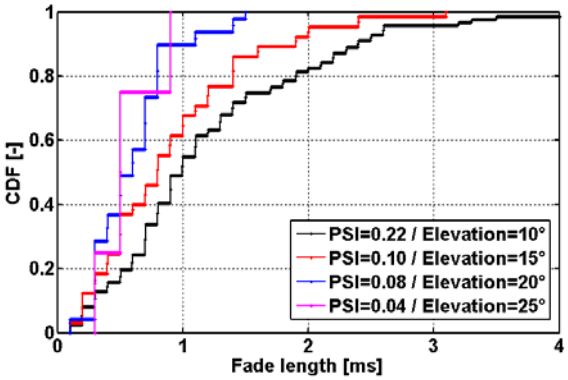

Fig. 11: Cumulative distribution functions for selected elevations in KT06-04. The fade threshold is defined as 3dB below instantaneous mean.

Related to fade frequency and fade duration is the fractional fade time. It quantifies the amount of bits in the data stream that are lost due to turbulence effects. In worst case situations identified in these measurements, fractional fade time may be up to 30%. But more frequent are cases between 1% and 10%. For code design, fade duration together with fractional fade time are useful for optimization. This part influences the code rate of the selected coding scheme.

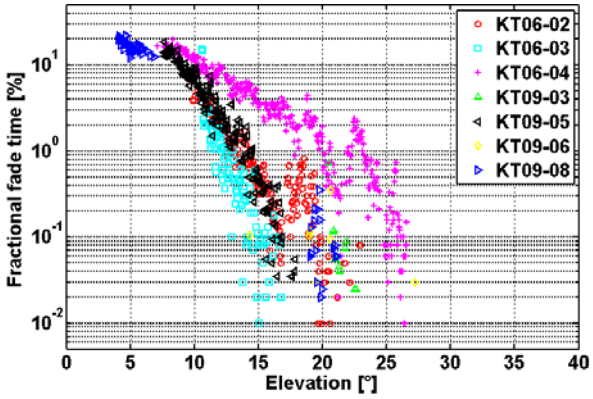

Fig. 12: Fractional fade time for all KIODO measurements. The fade threshold is defined as 3dB below instantaneous mean.

Altogether, the analysis of received power gives the direction in how to adjust receiver parameters, inter-leavers and coding schemes in this particular scenario. Interestingly, some trials, i.e. KT06-02 and KT06-04, reveal local maxima and minima in the presented curves. For the later, these are at around 18° and 23°.

Since power scintillation coincides with fade frequency, length, and time, local variation in C_n^2-profile are quite likely in charge of this phenomenon.

IV.II Shack-Hartmann wave-front sensor

The Shack-Hartmann wave-front sensor (SHWFS) of the OGS was designed to measure the phase of the incoming beam with high resolution (38x38 lens-lets) and sampling rate (1kHz). Each focus spot covers an area of about 12x12mm in the entrance pupil of the telescope. The intensity distribution can also be extracted from the SHS images. The wave-front was reconstructed from the phase slopes measured by the focus spot positions of the SHWFS lens-let array. A standard least-square reconstruction algorithm was used as explained e.g. in Hardy[19]. Fig. 13 on the left shows a typical image with the central telescope obscuration obtained from the SHS camera. On the right side the reconstructed wave-front is depicted. More details on the instrument, reconstruction algorithms, and specific issues to LEO downlinks can be found in Knapek[18].

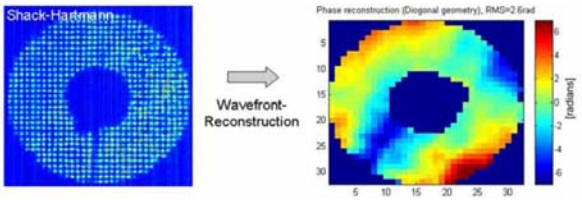

Fig. 13: Recorded Shack-Hartmann sensor image during a test link over 400m at 1064nm. Telescope spider, the central obscuration and the secondary-mirror drive can be seen. Right: Reconstructed wave-front.

Fig. 14 shows the phase probability density functions (PDF) from measurements recorded with the Shack-Hartmann sensor during the satellite-ground-link from OICETS during the measurement campaign 2009.

As a standard least-square reconstruction algorithm was used, it can be assumed that the phase values for elevation angles below 20 degrees elevation are underestimated due to strong scintillation effects and resulting phase singularities[20,21]. Barchers[17] analyzed the performance of Shack-Hartmann sensors in strong turbulence conditions. He observed a severe performance deterioration for a standard least-square reconstructor for Rytov indices $\sigma_R^2 > 0.2$, which comes with an increasing number of phase singularities. The deployment of a complex exponential reconstructor (CER)[22] was considered to improve the phase estimation accuracy. However, the CER algorithm only allows a performance improvement, if the ratio between the lens-let diameter d_L and the atmospheric coherence length r_0 is better $d_L / r_0 < 1/4$, which would require at least 160x160 lens-lets assuming a coherence length of 1cm. This could not be achieved with available cameras holding the requirement for a high frame-rate. Nevertheless, a comparison with theory and simulation based on standard models ($HV_{5/7}$) supported the qualitative validity of the measurement results.

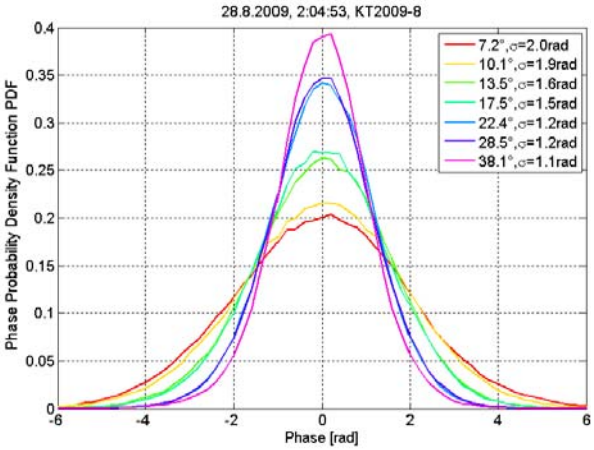

Fig. 14: Unwrapped phase PDF recorded by the Shack-Hartmann sensor during KT09-08. Several elevation angles are shown. 100 frames were averaged in a time window of 10s.

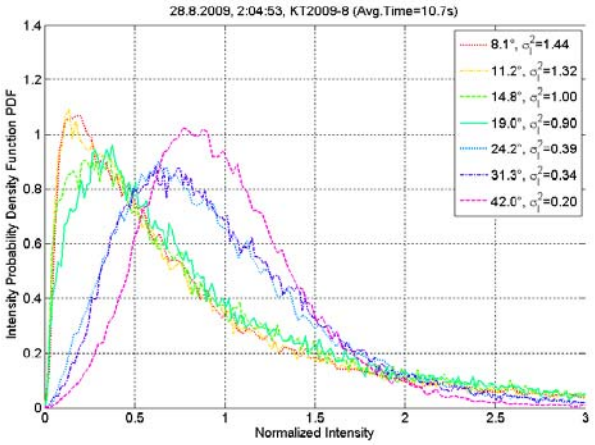

Fig. 15: Power PDF recorded with the Shack-Hartmann sensor during KT09-08. Several elevation angles are shown. 100 frames were averaged in a time window of 10s.

Fig. 15 shows the normalized power PDF measured with the Shack-Hartmann sensor. With a typical intensity correlation length (1/e point of the normalized covariance function) of the intensity speckles in the entrance pupil of several centimeters, the power PDF comes close to an intensity PDF. The shape at higher elevations tends towards a Gaussian distribution around intensity. Towards lower elevation angles, the shape becomes log-normal distributed, and then more and more similar to a negative-exponential distribution. The results compare well to the extended Rytov theory

developed by Andrews and Philips[23]. This theory is, in contrast to the classical weak intensity fluctuation theory, valid over all fluctuation regimes including strong fluctuations.

V Conclusion

Measurements of the communication channel for a LEO down-link to an optical ground station were achieved by employing various instruments. Out of these, the power and wave-front measurements are described in detail and results are presented. This analysis may be used as orientation for future systems that specify similar setups. It shows the combined effect of atmospheric turbulence and satellite slew rate on link behavior and also illustrates the dynamic of conditions a system experiences within individual or different flyovers. The statistics of power scintillation, temporal correlation and fading shall be used as a guideline for forthcoming inter-leaver and coding implementations. Furthermore, the Shack-Hartmann sensor analysis quantifies the wave-front distortions as these are necessary to know when dealing with free-space coupled coherent systems or single-mode fiber coupling. All these results lead to the suggestion of designing a system that can adapt its parameters like data-rate, code-rate, modulation scheme, inter-leaver size, etc. to the instantaneous channel state. Either open or closed loop algorithms are possible. An open loop system may employ measurements like the presented ones with which a look-up table can be created. The system parameters can then be optimized accordingly. A dynamic system could use an optical return channel to measure and calculate instantaneous atmospheric conditions. This return channel could be a radio frequency or optical link transmitting information from ground to the satellite. Also the received signal from the up-link tracking beacon may give valuable information about the channel state in the down-link. However, in this kind of channel sounding, investigation of up-/down-link correlation is necessary.

VI Acknowledgements

We want to acknowledge the excellent cooperation with JAXA (Japan Aerospace Exploration) and NICT (Japan National Institution of Information and Communication Technology) during the KIODO downlink campaigns in 2006 and 2009.

[1] European Space Agency, Space operations & situational awareness, " GMES/Sentinels," August 2011, http://www.esa.int/esaMI/Operations/SEM98Z8L6VE_0.html.

[2] European Space Agency, Telecommunications & integrated applications, "Sharing the satellite," August 2011, http://www.esa.int/esaTE/SEMWXV0T1PG_index_0.html.

[3] Y. Fujiwara et al, "Optical inter-orbit communications engineering test satellite (OICETS)," Acta Astronautica, vol. 61, pp. 163-175, 2007.

[4] T. Jono et al., "Overview of the inter-orbit and orbit-to-ground laser communication demonstration by OICETS," in Proceedings of SPIE, vol. 6457, 2007, pp. 645702-1 - 645702-10.

[5] M. Toyoshima, Y. Takayama, H. Kunimori, and T. Jono, "Data analysis results from KODEN experiments", in Proceedings of SPIE, vol. 6709, 2007, pp. 67091C-1 – 67091C-12.

[6] N. Perlot, M. Knapek, D. Giggenbach, J. Horwath, M. Brechtelsbauer, Y. Takayama, and T. Jono," Results of the optical downlink experiment KIODO from OICETS satellite to optical ground station Oberpfaffenhofen (OGS-OP)", in Proceedings of SPIE, vol. 6457, 2007, pp. 645704-1 - 645704-8.

[7] N. Perlot, "The Kirari optical downlink to Oberpfaffenhofen (KIODO)," German Aerospace Center (DLR), Weßling, Germany, Report on DLR-JAXA Joint Experiment, 2007.

[8] J. Kovalik, A. Biswas, K. Wilson, M. Wright, and W. T. Roberts,"Data products for the OCTL to OICETS optical link experiment", in Proceedings of SPIE, vol. 7587, 2010, pp. 75870C-1 – 75870C-12.

[9] Y. Takayama et al.,"Expanded laser communication demonstration with OICETS and ground stations", in Proceedings of SPIE, vol. 7587, 2010, pp. 75870D-1 - 75870D-8.

[10] K. E. Wilson, J. Kovalik, and A. Biswas," Preliminary results of the OCTL to OICETS optical link experiment (OTOOLE)", in Proceedings of SPIE, vol. 7587, 2010, pp. 75870D-1 - 75870D-8.

[11] F. Moll, "KIODO 2009: Trials and analysis," in International Workshop on Ground-to-OICETS Laser Communications Experiments 2010: GOLCE 2010, 2010, pp. 161-171.

[12] B. Epple, "Simplified Channel Model for Simulation of Free-Space Optical Communications," Journal of Optical Communications and Networking, vol. 2 (5), pp. 293-304, 2010.

[13] L. C. Andrews and R. L. Philips, Laser beam propagation through random media. Bellingham: SPIE Press, 2005.

[14] A. N. Kolmogorov, "The local structure of turbulence in incompressible fluids for very large Reynolds numbers," Proceedings of the Royal Society of London A, vol. 434, pp. 9-13, July 1991.

[15] M. Sarazin and F. Roddier, “The ESO differential image motion monitor,” in Astronomy and Astrophysics, Volume 227, Issue 1, pp. 294-300, 1990.

[16] W. M. Hughes and R. B. Holmes, "Pupil-plane imager for scintillometry over long horizontal paths," in Applied Optics, Volume 46, Issue 29, pp. 7099 – 7109, 2007.

[17] J. Barchers, D. Fried, and D. Link, “Evaluation of the performance of Hartmann sensors in strong scintillation,” Appl. Opt. **41**, No. 6 (2002).

[18] M. Knapek, Adaptive Optics for the Mitigation of Atmospheric Effects in Laser Satellite-To-Ground Communications, PhD Thesis, German Aerospace Center DLR, 2011.

[19] J. Hardy, *Adaptive Optics for Astronomical Telescopes* (Oxford University Press, 1998).

[20] D. Fried, “Branch point problem in adaptive optics,” J. Opt. Soc. Am. A **15** (1998).

[21] G. Tyler, “Reconstruction and assessment of the least-squares and slope discrepancy components of the phase,” J. Opt. Soc. Am. **17**, No.10 (2000).

[22] D. Fried, “Adaptive optics wave function reconstruction and phase unwrapping when branch points are present,” Opt. Commun. 200, Issues 1-6 (2001).

[23] L. Andrews, R. Philips, and C. Hopen, “Scintillation model for a satellite communication link at large zenith angles,” Opt. Eng. **39**, 3272-3280 (2000).